Research Article

Two-to-Two Processes at an Electron-Muon Collider

Antonio O. Bouzas [ID] and F. Larios [ID]

Departamento de Fsica Aplicada, CINVESTAV-Mérida, A.P. 73, 97310 Mérida, Yucatán, Mexico

Correspondence should be addressed to F. Larios; francisco.larios@cinvestav.mx

Based on a recent proposal to build an electron-muon collider, we study two-to-two production processes $e^- \mu^+ \longrightarrow f\bar{f}, \gamma\gamma$ that originate from dimension 6 and 8 operators. We compare the sensitivity to those effective couplings obtained at the collider with that of low energy measurements of $\mu \longrightarrow e\gamma$, $\mu \longrightarrow e\bar{e}e$, and $\mu \longrightarrow e$ conversion that have recently been reported in the literature. Whereas for the production of first family fermions, the sensitivity of the collider processes is much weaker; for the second and third family fermions, it is similar or stronger than that of low-energy processes. In the case of $e^- \mu^+ \longrightarrow \gamma\gamma$, the sensitivity to a dimension 8 contact operator turns out to be the strongest in comparison.

1. Introduction

With the main objective of measuring Higgs boson properties, there has been renewed interest in muon colliders [1–3]. At the low energy level, there have been numerous works concerning $(g-2)_\mu$ from the theoretical and experimental point of view [4–8]. In addition, the recent confirmation of a significant deviation from the Standard Model (SM) value of $(g-2)_\mu$ at Fermilab [9] has also encouraged the proposal of new physics models [10–17] as well as the calculation of higher order QED contributions to the $e\mu \longrightarrow e\mu$ scattering process [18, 19]. The idea of electron-muon collisions has been analyzed in past decades [20–25], and recently, it has been brought up again in a study of an extra Z' boson with generic couplings that could be searched for through a Lepton Flavor Violating (LFV) process like $e^- \mu^+ \longrightarrow e^+ \mu^-$ [26]. In a subsequent article, the construction of a high energy $e^- \mu^+$ collider has been proposed [27]. Besides the clear capability of probing muon LFV effects like the $He\mu$ coupling, this machine could even test the Higgs-bottom quark coupling [27]. One important advantage of such a machine is the very low level of SM background processes as they come mostly from vector boson fusion. Other than the elastic $e^- \mu^+ \longrightarrow e^- \mu^+$ there is no two-to-two process to contend

with, and this is what motivates our study. We are interested in fermion pair and two-photon production that can come from contact terms $e^- \mu^+ f\bar{f}$ and $e^- \mu^+ \gamma\gamma$.

LFV operators are already being strongly constrained from low energy measurements like muon decays and $\mu - e$ transitions [28–30]. We will show the comparison of the potential limits estimated here with these precision measurements. For $e^- \mu^+ \longrightarrow f\bar{f}$, we consider the four-fermion dimension-6 operators of the Standard Model Effective Field Theory (SMEFT) as given by the well known *Warsaw* basis [31]. We will also consider some dimension 8 operators that have been constrained in [29]. Given the chiral structure of the SMEFT, it is straightforward to obtain the corresponding amplitudes in the helicity basis. For the two-photon production $e^- \mu^+ \longrightarrow \gamma\gamma$, we address the contribution from the LFV dipole operator, that is very strongly constrained by $\mu \longrightarrow e\gamma$, and we consider as well a dimension 8 contact operator that is bound more strictly by our results than by low-energy measurements.

The paper is organized as follows. In Section 2, we analyze the two-body processes induced by four-fermion $e\mu f f$ operators. We explicity provide the corresponding helicity amplitudes and cross sections. Then, we estimate limits on the Wilson coefficients for 13 dimension 6 and 5 dimension 8 four-fermion operators. In Section 3, we consider $\gamma\gamma$

production originating from two different contributions: a trivalent dimension 6 dipole and a dimension 8 contact operator. We write down the sum of squared amplitudes and the total cross sections. We estimate limits on the coefficients in the same way we did in the previous section, but then, we carry out a detailed Monte Carlo analysis of signal and background processes. In this way, we show that our simplified strategy to obtain limits is realistic. Finally, in Section 4, we summarize our results.

2. Four Fermion Operators

Since we are dealing with massless chiral fermions, the amplitudes are most conveniently written in the helicity basis (see, for example, Ref. [32]). Assuming some degree of polarization in the incoming beams, the general form of the cross section can be divided in four terms:

$$
\sigma_{P_{e^-}P_{\mu^+}} = \frac{1 + \mathscr{P}_{e^-}}{2} \frac{1 + \mathscr{P}_{\mu^+}}{2} \sigma_{++} + \frac{1 - \mathscr{P}_{e^-}}{2} \frac{1 - \mathscr{P}_{\mu^+}}{2} \sigma_{--} \\
+ \frac{1 + \mathscr{P}_{e^-}}{2} \frac{1 - \mathscr{P}_{\mu^+}}{2} \sigma_{+-} + \frac{1 - \mathscr{P}_{e^-}}{2} \frac{1 + \mathscr{P}_{\mu^+}}{2} \sigma_{-+}. \quad (1)
$$

In this section, we will address four fermion contact operators, and we will obtain sensitivity limits with the following method: first, for each operator, we will assume a total polarization in the cross section. For instance, in $e_R^- \mu_R^+ \longrightarrow u_R \bar{u}_{eu}$ that comes from the right-chirality Q_{eu} operator, the $M(+ - + -)$ amplitude gives rise to the σ_{+-} cross section term, and we assume $\mathscr{P}_{e^-} = +1$, and $\mathscr{P}_{\mu^+} = -1$. Second, we neglect backgrounds and obtain sensitivities in optimal conditions. Third, we will assume an integrated luminosity of order $1ab^{-1}$ (as in Ref. [27]) and require a minimum cross section of $0.04 fb$ from the operator contribution. Such a cross section yields a significant amount of 40 events. In this way, since we are working with ideal conditions, we will avoid being too optimistic. There are 13 dimension 6 four-fermion operators and 9 of them only contribute to one of the four polarized cross sections. In their case, if there is only partial beam polarization the actual number of events could be reduced by about half or even by one quarter in case of unpolarized beams. On the other hand, we do not expect the presence of background to reduce the sensitivity significantly. In the next section, we will corroborate that this is true for $\gamma\gamma$ production, where we perform a full signal vs. background analysis.

2.1. Helicity Amplitudes. In this work, we are interested in the process $e^-(p_1)\mu^+(p_2) \longrightarrow f(p_3)\bar{f}(p_4)$ that does not exist in the SM at tree level, but that is generated by dimension six four-fermion operators in the SMEFT. Hereafter, $f\bar{f}$ will stand for any of the three charged leptons e, μ, and τ or any of the quarks except the top quark. The list of four fermion effective operators in Ref. [31] includes arbitrary (p, r, s, t) flavor indices to take into account. However, this does not mean that there are so many possible different helicity amplitudes as there are also Fierz identities that relate them. For instance, the operator $O_{ll} = \bar{l}_p \gamma_\nu l_r \bar{l}_s \gamma^\nu l_t$ gives rise to the

same amplitude $e^- \mu^+ \longrightarrow e^- e^+$ for any combination 2111, 1211, 1121, and 1112. We choose to work with 2111 that we denote as $O_{ll}^{2111} = \bar{l}_\mu \gamma_\nu l_e \bar{l}_e \gamma^\nu l_e$. For the processes $e^- \mu^+ \longrightarrow \mu^- \mu^+$ and $e^- \mu^+ \longrightarrow \tau^- \tau^+$, the amplitudes between O_{ll}^{2122} and O_{ll}^{2133} are clearly the same. In general, we shall take the flavor indices as 2111 for all the operators. This specific choice may exclude some other nonequivalent combinations in some operators, but we have found that this assignment, in the end, covers all the possible helicity amplitudes. The purpose of this preliminary study, rather than being comprehensive, is to get a first glimpse of the potential sensitivity of the $e^-\mu^+$ collider in two-to-two processes generated by contact operators and compare with the sensitivities of low energy measurements.

The helicity amplitudes are shown in Table 1. We see that $(\bar{L}L)(\bar{L}L)$ operators Q_{ll}, $Q_{lq}^{(1)}$, and $Q_{lq}^{(3)}$ generate exactly the same helicity amplitudes as they all involve left-chiral spinors. On the other hand, the $(\bar{L}L)(\bar{R}R)$ operator $Q_{ll} = \bar{l}_\mu \gamma_\mu l_e \bar{e}_e \gamma^\mu e_e$ gives rise to two possible combinations of final state chiralities: $e_R^- e_R^+$ and $e_R^- e_L^+$. They are not equivalent as shown in Table 1. Notice that many helicity amplitudes are actually equal up to a phase factor related to azimuthal angles. The phase factor is important only in the case of more than one diagram due to interference effects. We also point out that as a preliminary analysis, we will be considering the contribution of each operator separately. Because of the relations [32]:

$$
\langle ij \rangle = -\langle ji \rangle, [ij] = -[ji], \langle ij \rangle = [ji]^*, |\langle ij \rangle|^2 = 2p_i \cdot p_j, \quad (2)
$$

there are really only three different amplitude structures in this study: [12][34], [13][24], and [14][23]. Their squares are proportional to the Mandelstam s^2, t^2, and u^2, respectively. So, they are actually not independent. In fact, there is an identity that is easy to verify [32]: [12][34] = [14][32] + [13][24].

Now let us turn our attention to dimension 8 operators. There are multiple structures, but we will pay attention to those specific operators that have been bounded from $\mu \longrightarrow e$ processes [28, 29]. Moreover, there are dimension 8 operators that coincide with some dimension 6 operator except for an additional $H^\dagger H$ term. Obviously, their amplitudes would be equal except for some rescaling factor. The amplitudes of the dimension 8 operators that give rise to chiral structures that do not appear at dimension 6 are shown in Table 2.

2.2. Cross Sections and Limits on Coefficients. As mentioned above, there are only three different types of helicity amplitudes squared. Each of them gives rise to one specific expression for the cross section. For $|[12][34]|^2 = s^2$, after dividing by the energy scale Λ^4 and integrating over the phase space we obtain: $\sigma_{1234} = s/(16\pi\Lambda^4)$. For the center-of-mass (CM) collider energy $\sqrt{s} = 1.095 \, \text{TeV}$ ($E_e = 100$, $E_\mu = 3000 \, \text{GeV}$), we obtain $\sigma_{1234}(\sqrt{s} = 1.095 \, \text{TeV}) = 36.3 \, \text{fb}$. We will show the corresponding cross sections for each operator in terms of this common σ_{1234}. The other amplitudes yield $\sigma_{1324} =$

TABLE 1: Dimension 6 operators with common flavor indices (2111) and the helicity amplitudes generated. The C_O/Λ^2 factor to be included. The R, L indices refer to chiralities. Final state e^-e^+ also stands for $\mu^-\mu^+$ and $\tau^-\tau^+$. Similarly, $d\bar{d}$ also stands for $s\bar{s}$ and $b\bar{b}$, and $u\bar{u}$ also stands for $c\bar{c}$. Top quarks excluded.

	$(\bar{L}L)(\bar{L}L)$	$e^-(p_1)\mu^+(p_2) \longrightarrow f(p_3)\bar{f}(p_4)$	$\mathcal{M}$
O_{ll}	$\bar{l}_\mu \gamma_\nu l_e \bar{l}_e \gamma^\nu l_e$	$e^-_L \mu^+_L \longrightarrow e^-_L e^+_L$	$2[14]\langle 32\rangle$
$O_{lq}^{(1)}$	$\bar{l}_\mu \gamma_\nu l_e \bar{q}\gamma^\nu q$	$e^-_L \mu^+_L \longrightarrow u_L \bar{u}_L$	$2[14]\langle 32\rangle$
$O_{lq}^{(3)}$	$\bar{l}_\mu \gamma_\nu \tau^I l_e \bar{q}\gamma^\nu \tau^I q$	$e^-_L \mu^+_L \longrightarrow u_L \bar{u}_L, d_L \bar{d}_L$	$\mp 2[14]\langle 32\rangle$
	$(\bar{R}R)(\bar{R}R)$	$e^-(p_1)\mu^+(p_2) \longrightarrow f(p_3)\bar{f}(p_4)$	$\mathcal{M}$
O_{ee}	$\bar{e}_\mu \gamma_\nu e_e \bar{e}_e \gamma^\nu e_e$	$e^-_R \mu^+_R \longrightarrow e^-_R e^+_R$	$2\langle 14\rangle[32]$
O_{eu}	$\bar{e}_\mu \gamma_\nu e_e \bar{u}\gamma^\nu u$	$e^-_R \mu^+_R \longrightarrow u_R \bar{u}_R$	$2\langle 14\rangle[32]$
O_{ed}	$\bar{e}_\mu \gamma_\nu e_e \bar{d}\gamma^\nu d$	$e^-_R \mu^+_R \longrightarrow d_R \bar{d}_R$	$2\langle 14\rangle[32]$
	$(\bar{L}L)(\bar{R}R)$	$e^-(p_1)\mu^+(p_2) \longrightarrow f(p_3)\bar{f}(p_4)$	$\mathcal{M}$
O_{le}	$\bar{l}_\mu \gamma_\nu l_e \bar{e}_e \gamma^\nu e_e$	$e^-_L \mu^+_L \longrightarrow e^-_R e^+_R$	$2\langle 24\rangle[31]$
O_{le}	$l_\mu \gamma_\nu l_e \bar{e}_e \gamma^\nu e_e$	$e^-_R \mu^+_L \longrightarrow e^-_R e^+_L$	$2\langle 21\rangle[34]$
O_{lu}	$l_\mu \gamma_\nu l_e \bar{u}\gamma^\nu u$	$e^-_L \mu^+_L \longrightarrow u_R \bar{u}_R$	$2\langle 24\rangle[31]$
O_{ld}	$l_\mu \gamma_\nu l_e \bar{d}\gamma^\nu d$	$e^-_L \mu^+_L \longrightarrow d_R \bar{d}_R$	$2\langle 24\rangle[31]$
O_{qe}	$\bar{q}\gamma_\nu q \bar{e}_u \gamma^\nu e_e$	$e^-_R \mu^+_R \longrightarrow u_L \bar{u}_L, d_L \bar{d}_L$	$2[24]\langle 31\rangle$
	$(\bar{L}R)(\bar{R}L)$	$e^-(p_1)\mu^+(p_2) \longrightarrow f(p_3)\bar{f}(p_4)$	$\mathcal{M}$
O_{ledq}	$\bar{l}_\mu e_e \bar{d}q$	$e^-_R \mu^+_L \longrightarrow d_R \bar{d}_L$	$[12][43]$
	$(\bar{L}R)(\bar{L}R)$	$e^-(p_1)\mu^+(p_2) \longrightarrow f(p_3)\bar{f}(p_4)$	$\mathcal{M}$
$O_{lq}^{(1)}$	$\bar{l}_\mu^j e_e \varepsilon_{jk}\bar{q}^k u$	$e^-_R \mu^+_L \longrightarrow u_R \bar{u}_L$	$\langle 12\rangle[34]$
$O_{lequ}^{(3)}$	$\bar{l}_\mu^j \sigma_{\mu\nu} e_e \varepsilon_{jk}\bar{q}^k \sigma^{\mu\nu} u$	$e^-_R \mu^+_L \longrightarrow u_R \bar{u}_L$	$4([13][24]+[14][23])$

TABLE 2: Helicity amplitudes generated by dimension 8 operators with common flavor indices (2111) associated to four-fermion contact vertices that do not appear with dimension 6 operators. A $(v^2/2)(C_O/\Lambda^4)$ factor is to be included. As in Table 1, final state e^-e^+ also stands for $\mu^-\mu^+$ and $\tau^-\tau^+$, $d\bar{d}$ also stands for $s\bar{s}$ and $b\bar{b}$, and $u\bar{u}$ also stands for $c\bar{c}$.

	$(\bar{L}R)(\bar{L}R)$	$e^-(p_1)\mu^+(p_2) \longrightarrow f(p_3)\bar{f}(p_4)$	$\mathcal{M}$
$O_{le}^{(8)}$	$\bar{l}_\mu H e_e \bar{l}_e H e_e$	$e^-_R \mu^+_L \longrightarrow e^-_R e^+_L$	$\langle 12\rangle[43]$
$O_{Tle}^{(8)}$	$\bar{l}_\mu H \sigma^{\mu\nu} e_e \bar{l}_e H \sigma_{\mu\nu} e_e$	$e^-_R \mu^+_L \longrightarrow e^-_R e^+_L$	$4([31][24]+[41][23])$
$O_{leqd1}^{(8)}$	$\bar{l}_\mu H e_e \bar{q}H d$	$e^-_R \mu^+_L \longrightarrow d_R \bar{d}_L$	$\langle 12\rangle[43]$
$O_{leqd3}^{(8)}$	$\bar{l}_\mu H \sigma^{\mu\nu} e_e \bar{q}H \sigma_{\mu\nu} d$	$e^-_R \mu^+_L \longrightarrow d_R \bar{d}_L$	$4([31][24]+[41][23])$
$O_{le}^{(8)}$	$\bar{l}_\mu H e_e \bar{l}_e H e_e$	$e^-_R \mu^+_L \longrightarrow e^-_L e^+_R$	$\langle 24\rangle[31]$
$O_{Tle}^{(8)}$	$\bar{l}_\mu H \sigma^{\mu\nu} e_e \bar{l}_e H \sigma_{\mu\nu} e_e$	$e^-_R \mu^+_L \longrightarrow e^-_L e^+_R$	$4([21][34]+[14][23])$
	$(\bar{L}R)(\bar{R}L)$	$e^-(p_1)\mu^+(p_2) \longrightarrow f(p_3)\bar{f}(p_4)$	$\mathcal{M}$
$O_{leuq}^{(8)}$	$\bar{l}_\mu H e_e \bar{u}\tilde{H}^\dagger q$	$e^-_R \mu^+_L \longrightarrow u_R \bar{u}_L$	$\langle 12\rangle\langle 43\rangle$

$\sigma_{1423} = \sigma_{1234}/3$. The amplitudes obtained here grow with the collision energy, but our effective theory calculation is valid for energies below the cut-off scale $\Lambda = 4\,\text{TeV}$.

Three benchmark collision energies are proposed in [27]: (1) $E_e = 20$, $E_\mu = 200\,\text{GeV}$; (2) $E_e = 50$, $E_\mu = 1000\,\text{GeV}$; and (3) $E_e = 100$, $E_\mu = 3000\,\text{GeV}$ that correspond to CM energies of $\sqrt{s} = 2\sqrt{E_e E_\mu} = 0.126, 0.447, 1.095\,\text{TeV}$, respectively. Since all cross sections are proportional to $s|C_O|^2$ computing the bound at an energy $\sqrt{s_2}$ assuming we know the bound at an energy $\sqrt{s_1}$ is straigthforward: we just multiply by the

TABLE 3: Upper limits to the dimension 6 coefficients from the low energy experiments as reported in Tables 6 and 7 of [28]. They have been multiplied by a factor $(4/0.174)^2$ to account for the normalization scale m_t used by [28] instead of the $\Lambda = 4\,\text{TeV}$ scale adopted in this study. In addition, the ratio of limits Low/Collider is shown in parenthesis ($E_e = 100$, $E_\mu = 3000$ GeV).

C_Q	C_Q^{Low} ($C^{\text{Low}}/C^{\text{Coll}}$) e^-e^+	C_Q^{Low} ($C^{\text{Low}}/C^{\text{Coll}}$) $\mu^-\mu^+$	C_Q^{Low} ($C^{\text{Low}}/C^{\text{Coll}}$) $\tau^-\tau^+$
C_{ll}	$4.16 \times 10^{-4}\,(1.45 \times 10^{-2})$	$0.98 \times 10^{-2}\,(0.34)$	$1.97 \times 10^{-2}\,(0.69)$
C_{ee}	$4.16 \times 10^{-4}\,(1.45 \times 10^{-2})$	$0.98 \times 10^{-2}\,(0.34)$	$1.97 \times 10^{-2}\,(0.69)$
C_{le}	$4.92 \times 10^{-4}\,(2.96 \times 10^{-2})$	$1.99 \times 10^{-2}\,(1.20)$	$1.98 \times 10^{-2}\,(1.19)$
	$d\bar{d}$	$s\bar{s}$	$b\bar{b}$
$C_{lq}^{(1)}$	$1.51 \times 10^{-5}\,(0.91 \times 10^{-3})$	$1.60 \times 10^{-2}\,(0.96)$	$2.49 \times 10^{-2}\,(1.50)$
$C_{lq}^{(3)}$	$2.69 \times 10^{-4}\,(1.62 \times 10^{-2})$	$6.08 \times 10^{-3}\,(0.37)$	$2.49 \times 10^{-2}\,(1.50)$
C_{ld}	$2.80 \times 10^{-5}\,(1.69 \times 10^{-3})$	$1.97 \times 10^{-2}\,(1.19)$	$2.49 \times 10^{-2}\,(1.50)$
C_{ed}	$2.86 \times 10^{-5}\,(1.72 \times 10^{-3})$	$1.97 \times 10^{-2}\,(1.19)$	$2.49 \times 10^{-2}\,(1.50)$
C_{qe}	$1.52 \times 10^{-5}\,(0.92 \times 10^{-3})$	$1.58 \times 10^{-2}\,(0.95)$	$2.50 \times 10^{-2}\,(1.51)$
C_{ledq}	$5.34 \times 10^{-6}\,(2.79 \times 10^{-4})$	$1.11 \times 10^{-4}\,(5.80 \times 10^{-3})$	$3.66 \times 10^{-3}\,(0.19)$
	$u\bar{u}$	$c\bar{c}$	$--$
C_{lu}	$3.30 \times 10^{-5}\,(1.99 \times 10^{-3})$	$0.88 \times 10^{-2}\,(0.53)$	
C_{eu}	$3.19 \times 10^{-5}\,(1.92 \times 10^{-3})$	$0.89 \times 10^{-2}\,(0.54)$	
$C_{lequ}^{(1)}$	$5.45 \times 10^{-6}\,(2.84 \times 10^{-4})$	$0.97 \times 10^{-3}\,(5.1 \times 10^{-2})$	
$C_{lequ}^{(3)}$	$5.10 \times 10^{-5}\,(6.1 \times 10^{-3})$	$5.34 \times 10^{-6}\,(6.4 \times 10^{-4})$	

ratio $\sqrt{s_1}/\sqrt{s_2}$. For instance, $0.447/1.095 = 0.4$, and so we see that the limits at benchmark (3) will be more than twice stronger than benchmark (2). We shall focus on the $E_e = 100$, $E_\mu = 3000$ GeV benchmark in this study. However, in Section 3, we will see that the cross sections for $e^-\mu^+ \longrightarrow \gamma\gamma$ are not proportional to s, but one is constant in energy, and the other is proportional to s^2. We will provide limits obtained with the benchmark (3) $E_e = 100$, $E_\mu = 3000$ GeV and for greater energies.

The dimension 6 operators of Table 1 yield the following cross sections:

$$\frac{\sigma_{++}}{\sigma_{1234}} = 4|C_{le}|^2 + N_c|C_{ledq}|^2 + N_c\left|C_{lequ}^{(1)}\right|^2 + \frac{16}{3}N_c\left|C_{lequ}^{(3)}\right|^2,$$

$$\frac{\sigma_{+-}}{\sigma_{1234}} = \frac{4}{3}|C_{ee}|^2 + \frac{4}{3}N_c|C_{eu}|^2 + \frac{4}{3}N_c|C_{ed}|^2 + \frac{4}{3}N_c|C_{qe}|^2,$$

$$\frac{\sigma_{-+}}{\sigma_{1234}} = \frac{4}{3}|C_{ll}|^2 + \frac{4}{3}|C_{le}|^2 + \frac{4}{3}N_c\left|C_{lq}^{(1)}\right|^2 + \frac{4}{3}N_c\left|C_{lq}^{(3)}\right|^2$$
$$+ \frac{4}{3}N_c|C_{lu}|^2 + \frac{4}{3}N_c|C_{ld}|^2,$$

(3)

where the σ_{--} term does not appear for the flavor assignment 2111, but the operators that generate σ_{++} would also generate σ_{--} with the assignment 1211.

By requiring that the value of a C_Q coefficient be enough to yield the minimum 0.04 fb of production cross section, we obtain the following lower limits for $E_e = 100$, $E_\mu = 3000$ GeV:

$$C_{ll}, C_{ee} \geq 2.88 \times 10^{-2},$$

$$C_{le}, C_{lu}, C_{ld}, C_{qe} \geq 1.66 \times 10^{-2},$$

$$C_{eu}, C_{ed}, C_{lq}^{(1)}, C_{lq}^{(3)} \geq 1.66 \times 10^{-2},$$

$$C_{lequ}^{(3)} \geq 0.83 \times 10^{-2}.$$

(4)

We can compare with the limits from low energy processes $\mu \longrightarrow e\gamma$, $\mu \longrightarrow e\bar{e}e$, and $\mu \longrightarrow e$ conversion in nuclei $\mu A \longrightarrow eA$ as recently reported in Tables 6 and 7 of Ref. [28]. We would like to point out that in almost all cases the most stringent bounds in those tables come from $\mu A \longrightarrow eA$ conversion in nuclei [33]. The exceptions are first family four-lepton coefficients C_{ll}, C_{le}, C_{ee} that are constrained by $\mu \longrightarrow e\bar{e}e$ (Tables 6 [28]) and $C_{lequ}^{(3)e\mu cc}$ that is constrained by $\mu \longrightarrow e\gamma$ (Table 7 [28]). Moreover, these $\mu A \longrightarrow eA$ bounds are in fact around four orders of magnitude stronger than the ones from $\mu \longrightarrow e\gamma$ and $\mu \longrightarrow e\bar{e}e$. This brings up one important observation: that if we ignored $\mu A \longrightarrow eA$, the conclusion would be that the $e\mu$ collider would yield much stronger constraints than any of the low energy measurements. In Table 3, we show the limits to each

operator coefficient (at the scale m_W) and the ratio $C_Q^{\text{Low energy}}/C_Q^{\text{Collider}}$ for each possible final state. Not surprisingly, we can observe that for the first family fermions the limits are very stringent. However, for the second and third family modes that get their low energy limits via loop contributions, the bounds are weaker and about the same order of magnitude as the potential limits from the $e^-\mu^+ \longrightarrow f\bar{f}$ production. Strictly speaking, the collider sensitivity for each coefficient is taken at a scale of order 1 TeV, about ten times higher than the electroweak scale. In a more precise analysis, one should take into account the renormalization group dependence on the scale. However, one should bear in mind that such corrections are usually of order a few percent. For instance, the coefficient C_{DL} associated to the operator: $(C_{DL}m_\mu/m_t^2)\bar{e}_R\sigma^{\mu\nu}\mu_L F^{\mu\nu}$. An upper limit from its contribution to $\mu \longrightarrow e\gamma$ decay is reported as $|C_{DL}| < 1.05 \times 10^{-8}$ at the muon mass scale [28]. The same limit becomes $|C_{DL}| < 1.12 \times 10^{-8}$ at the m_W scale, which is only a 7% numerical variation. For another example, let us consider the dimension 6 coefficient C_{el} above. In a series of articles [34–37], we can find the renormalization group evolution of the dimension 6 SMEFT operators listed in the Warsaw basis. The running of C_{el} in general depends on several other operators, but let us take the term proportional to C_{el} itself. Then, we find that $C_{le}(1\,\text{TeV}) \sim 0.96 C_{le}(m_W)$, that is only a 4% correction. As we are only interested in a preliminary assessment of sensitivities and comparisons with low energy experiment limits, we shall not take corrections of scale dependence into account. Recently, limits on the $C_{lq}^{(1)}$ and $C_{lq}^{(3)}$ coefficients have been published based on the LHC $pp \longrightarrow e\mu$ dilepton production that are approximately $C_{lq}^{(1,3)} < 0.3$ for first family quarks, $C_{lq}^{(1,3)} < 2.0$ for second family, and $C_{lq}^{(1,3)} < 5.0$ for $b\bar{b}$ [38]. They project that with a hundred times more luminosity the HL-LHC could reduce these limits to one-third of the current value. From what we have found here, the $e\mu$ collider would have at least one order of magnitude greater sensitivity than the HL-LHC for these operators.

The dimension 8 operators of Table 2 yield the following cross sections:

$$\frac{\sigma_{++}}{\sigma_{1234}}(e_R^-e_L^+) = \frac{v^4}{4\Lambda^4}\left(\left|C_{le}^{(8)}\right|^2 + N_c\left|C_{leqd1}^{(8)}\right|^2 + N_c\left|C_{leuq}^{(8)}\right|^2\right.$$
$$\left. + \frac{16}{3}N_c\left|C_{leqd3}^{(8)}\right|^2 + \frac{16}{3}\left|C_{Tle}^{(8)}\right|^2\right),$$

$$\frac{\sigma_{++}}{\sigma_{1234}}(e_L^-e_R^+) = \frac{v^4}{4\Lambda^4}\left(\frac{1}{3}\left|C_{le}^{(8)}\right|^2 + \frac{112}{3}N_c\left|C_{Tle}^{(8)}\right|^2\right).$$

(5)

A comment on the tensor operators $Q_{lequ}^{(3)}$, Q_{leqd3}, and Q_{Tle} is in order here. $Q_{lequ}^{(3)}$, Q_{leqd3}, and the $\sigma_{++}(e_R^-e_L^+)$ contributions of Q_{Tle} generate the same amplitude $[13][24] + [14][23]$. Except for the $v^4/(4\Lambda^4)$ additional factor, the cross sections are equal. However, for the $\sigma_{+-}(e_L^-e_R^+)$ helicity mode,

C_Q	$C^{\text{Low}}/C^{\text{Coll}}$
$C_{le}^{(8)}$	$5 \times 10^{-3}/14.0$
$C_{Tle}^{(8)}$	$2 \times 10^{-3}/1.3$
$C_{leqd1}^{(8)}$	$3 \times 10^{-5}/8.1$
$C_{leqd3}^{(8)}$	$7 \times 10^{-4}/3.5$
$C_{leuq}^{(8)}$	$3 \times 10^{-5}/8.1$

the Q_{Tle} amplitude is $[21][34] + [14][23]$. In the CM frame, the functional dependence on the p_3 polar angle's $\cos\theta$ is $[13][24] + [14][23] \sim \cos\theta$. If we compare with $[21][34] + [14][23] \sim (3 + \cos\theta)/2$, we can see that the latter yields a much greater cross section.

As in Table 3 and in Table 4, we show the ratio $C^{\text{Low}}/C^{\text{Coll}}$ for the dimension 8 operators. Comparing with the dimension 6 coefficients, there is a suppresing $v^2/(2\Lambda^2)$ factor of order 2×10^{-3}, and the C^{Coll} minimum values have to be much bigger. In contrast, according to Table 5 of Ref. [29], the limits from low energy experiments are still very stringent for dimension 8 couplings.

What we have learned from Table 3 is that for first family fermions $f\bar{f}$ the sensitivity of the low energy measurement of $\mu A \longrightarrow eA$ conversion in nuclei is two or more orders of magnitude higher. Maybe all the operator coefficients are indeed very suppressed, regardless of potential cancellations. However, for most of the second and third family $f\bar{f}$ states, the collider sensitivities are of the same order of magnitude as the low energy limits. The electron-muon collider should be able to provide additional and competitive limits to constrain the set of dimension 6 four fermion LFV operators. The same may not be true for dimension 8 operators, at least for the ones that can be constrained by the low energy experiments.

3. The $e^-\mu^+ \longrightarrow \gamma\gamma$ Process

The $e^-\mu^+ \longrightarrow \gamma\gamma$ amplitude can be generated by the dimension 6 flavor-changing magnetic dipole operator

$$Q_{eA} = \bar{l}_\mu\sigma^{\mu\nu}e_e H F_{\mu\nu},$$

(6)

through t and u channel diagrams where one of the photons is emitted by the effective coupling. Another possibility comes from the dimension 8 operator

$$Q_{eAA} = \bar{l}_\mu e_e H F^{\mu\nu} F_{\mu\nu}.$$

(7)

We have two chiral versions: Q_{eAL} and Q_{eAR} (Q_{eAAL}, Q_{eAAR}) referring to left-handed and right-handed electron, respectively. In Figure 1, we show the Feynman diagrams associated to each operator.
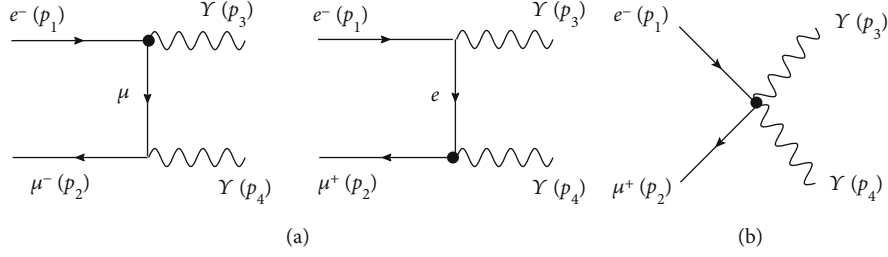
FIGURE 1: The anomalous two-to-two process $e^-\mu^+ \longrightarrow \gamma\gamma$. Process (a) ($t$-channel) as given by the trivalent vertex dipole operator Q_{eA}. Process (b) as given by the contact term, dimension 8 operator Q_{eAA}.

Both operators give rise to amplitudes that do not depend on angles:

$$\sum |M|^2 = \left(|C_{eAL}|^2 + |C_{eAR}|^2\right) e^2 \frac{v^2}{\Lambda^4} 48s$$
$$+ \left(|C_{eAAL}|^2 + |C_{eAAR}|^2\right) \frac{v^2}{\Lambda^8} 4s^3. \tag{8}$$

They yield the total cross sections:

$$\sigma_{--} + \sigma_{++} = \left(|C_{eAL}|^2 + |C_{eAR}|^2\right) \frac{3e^2 v^2}{2\pi \Lambda^4}$$
$$= \left(|C_{eAL}|^2 + |C_{eAR}|^2\right) 4.32 \, \text{fb}, \tag{9}$$

$$\sigma_{--} + \sigma_{++} = \left(|C_{eAAL}|^2 + |C_{eAAR}|^2\right) \frac{v^2}{8\pi \Lambda^8} s^2$$
$$= \left(|C_{eAAL}|^2 + |C_{eAAR}|^2\right) 0.0206 \, \text{fb}, \tag{10}$$

where the numerical value on the first line is independent of the collision energy, but the numerical value on the second line is taken at $\sqrt{s} = 1.095 \, \text{TeV}$.

We see, then, that coefficients $C_{eAL(R)}$ and $C_{eAAL(R)}$ of order 0.1 and $\sqrt{2}$, respectively, would give us a $\sigma = 0.04$ fb value that is our minimum acceptable cross section. Let us notice that the current limit from $\mu \longrightarrow e\gamma$ is of order 5×10^{-6} for the dipole coefficient $C_{eAL(R)}$, well below the potential collider sensitivity. On the other hand, for the dimension 8 operator coefficient $C_{eAAL(R)}$, the potential sensitivity from $\mu A \longrightarrow eA$ transitions is six orders of magnitude less stringent: $C_{eAAL(R)} \leq 3.2$ [29]. We point out that, in this study, this last coefficient is the one with the highest sensitivity by the $e\mu$ collider as compared to the low energy measurements.

Seeing the relatively high sensitivity to the electromagnetic Q_{eAA} operator, one may wonder what about the effective vertex $e\mu GG$? We can use the Q_{eAA} calculation with the analogous gluon operator

$$Q_{eGG} = \frac{C_{eGG}}{\Lambda^4} \bar{l}_\mu e_e H G^{a\mu\nu} G^a_{\mu\nu}. \tag{11}$$

The $e^-\mu^+ \longrightarrow gg$ production cross section is now $N_c = 8$ times greater than $e^-\mu^+ \longrightarrow \gamma\gamma$, and a coefficient of order 0.5 would yield the minimum observable production. However, according to [29], the low energy $\mu A \longrightarrow eA$ limit is three

orders of magnitude more stringent in this case: $C_{eGG} \leq 1.6 \times 10^{-3}$.

As mentioned above, the amplitudes squared for $e^-\mu^+ \longrightarrow \gamma\gamma$ do not depend on the polar angle. That means that in terms of rapidity, for instance, $y = y_3^*$ in the CM frame:

$$\frac{d\sigma}{dy} = \frac{d\sigma}{dc_\theta}\frac{dc_\theta}{dy} = a_0 \frac{4 \exp(2y)}{(1 + \exp(2y))^2}, \tag{12}$$

where a_0 is a constant. The shape of the rapidity distribution in the CM frame is then centered around zero with a width of approximately 2 units. In the lab frame, the center is shifted towards -1.70 (see next subsection).

3.1. Monte Carlo Analysis of $\gamma\gamma$ Production and Its SM Background.
In the SM, $\gamma\gamma$ production is given by the two-to-four process $e^-\mu^+ \longrightarrow \gamma\gamma\nu_e\bar{\nu}_\mu$, involving 13 Feynman diagrams in unitary gauge. There is also e^-e^+ production $e^-\mu^+ \longrightarrow \nu_e\bar{\nu}_\mu e^-e^+$, involving 24 Feynman diagrams. In Figure 2, we show two representative diagrams for the $\gamma\gamma$ and resonant e^-e^+ production in the SM. Signal and background have very different kinematics, and this makes the separation straightforward. Our goal is to show how a basic set of cuts can reduce the potential background dramatically. We point out here that in the lab frame the rapidities y are shifted with respect to those y^* in the CM frame:

$$y = y^* - y_0, \text{with } y_0 = \frac{1}{2} \ln\left(\frac{E_\mu}{E_e}\right) = 1.70, \tag{13}$$

where $y_0 = 1.7$ is the shift value for $E_\mu/E_e = 30$. The muon beam goes in the direction of $-\hat{k}$, and so the event products usually appear on the backward hemisphere.

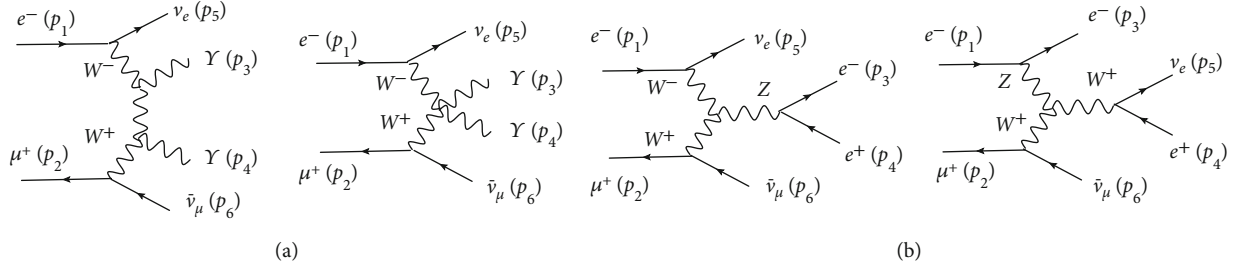Thus, to study $\gamma\gamma$ production in $e^-\mu^+$ collisions, we consider the three processes,

$$e^-\mu^+ \longrightarrow \gamma\gamma, \tag{14}$$

$$e^-\mu^+ \longrightarrow \gamma\gamma\bar{\nu}_\mu\nu_e, \tag{15}$$

$$e^-\mu^+ \longrightarrow e^-e^+\bar{\nu}_\mu\nu_e, \tag{16}$$

where the first one is our signal process as depicted in Figure 1 and (15) and (16) the SM backgrounds shown in Figure 2. We implemented the effective interactions (6) and (7) in our Monte Carlo simulations by means of

FIGURE 2: Representative unitary-gauge Feynman diagrams for the SM processes (a) $e^-\mu^+ \longrightarrow \gamma\gamma\nu_e\bar{\nu}_\mu$ and (b) $e^-\mu^+ \longrightarrow e^-e^+\nu_e\bar{\nu}_\mu$.

— Eq. (10)   — Eq. (8)
— Eq. (11)   — Eq. (12)
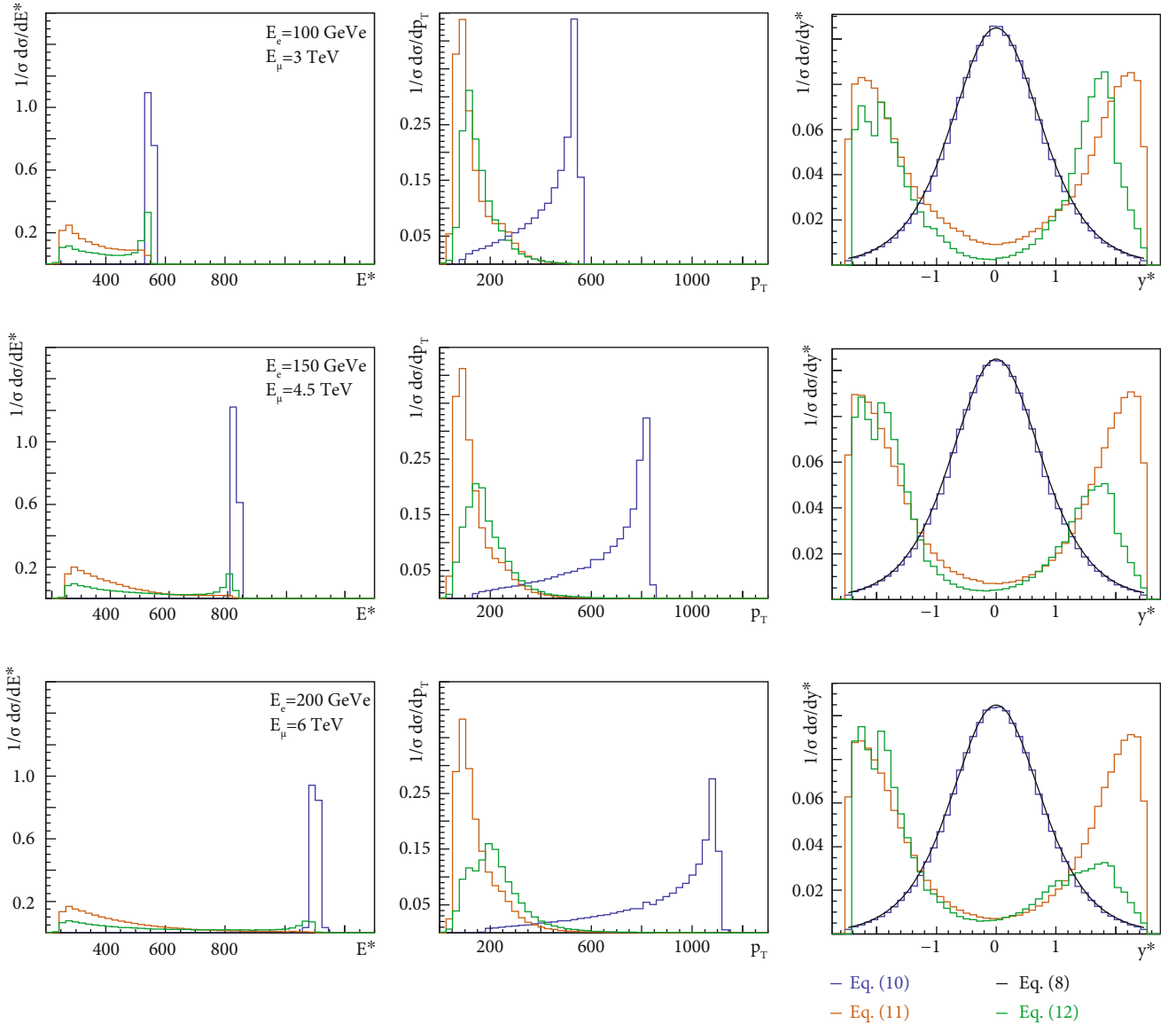
FIGURE 3: Normalized differential cross sections for final-state photons for processes (14) and (15) and $e^\pm$ for process (16), with respect to center-of-mass energy (a), transverse momentum (b), and center-of-mass rapidity (c). The beam energies are $(E_e, E_\mu) = (100\,\text{GeV}, 3\,\text{TeV})$ (upper row), (150 GeV, 4.5 TeV) (middle row), and (200 GeV, 6 TeV) (lower row). Blue lines: signal process (14); black line: analytical expression (12); orange lines: background process (15); green lines: background process (16). All differential cross section correspond to detector-level events with cuts (18).

feynrules 2.0 [39]. We simulated the signal and background processes with madgraph 2.6 [40], with beam energies $(E_e, E_\mu) = (100, 3000)$, $(150, 4500)$, and $(200, 6000)$ GeV. We then have $\sqrt{s} = 1.095$, 1.643, and 2.191 TeV, respectively. In the two-body signal process (14), the CM energies of the final photons are fixed at $E_3^* = E_4^* = \sqrt{s}/2$. This is unlike what happens with the backgrounds (15) and (16), where there is a continuous spectrum for E_3^* and E_4^*. Similarly, for the signal process $|\vec{p}_{3T} + \vec{p}_{4T}| = 0$, but for the backgrounds $|\vec{p}_{3T} + \vec{p}_{4T}| = E_T$ which has a continuous range of values. Furthermore, we observe the final-state photons in the signal process to be very central in the CM frame, with $|y_{3,4}^*| = |y_{3,4} + y_0| \lesssim 2.5$ for the vast majority of events, as expected in view of the analytical distribution (12) and as shown in Figure 3. For the process (15), without restrictions on $E_{3,4}^*$, the photon rapidity distribution in the lab frame is symmetric about $-y_0 = -1.70$, but very broad. If we require $E_{3,4}^*$ in (15) to be large, however, the final-state photons must be very forward or backward. For example, if $E_{3,4}^* \simeq 250$ GeV, the rapidities will have maxima at $-y_0 \pm \Delta y$ with $\Delta y \simeq 2$ as shown in Figure 3, and Δy gets larger for greater values of $E_{3,4}^*$. For the process (16), the electron rapidity distribution presents essentially the same features but is less forward-backward symmetric, as seen in the figure.

We are, thus, led to consider the following set of phase-space cuts,

$$
\begin{aligned}
C_0 &: p_{3T}, p_{4T} > 1.0\,\text{GeV}, \\
C_1 &: E_3^*, E_4^* > 500.0\,\text{GeV}, \\
C_2 &: p_T^{\text{tot}} = \left|\vec{p}_{3T} + \vec{p}_{4T}\right| < 20.0\,\text{GeV}, \\
C_3 &: |y_3 + y_0|, |y_4 + y_0| < 1.75.
\end{aligned}
\tag{17}
$$

The cut C_0 is necessary to control infrared divergences in (15) and (16). As discussed above, the cuts $C_{1,2,3}$ in (17) have only small effects on the signal cross section, but they do substantially decrease the cross section for the backgrounds. The effect of the cuts (17) on the cross sections for the processes (14), (15), and (16) is illustrated at $(E_e, E_\mu) = (100, 3000)$ GeV in Table 5. The cross section $\sigma_{\gamma\gamma}^{(3)}$ refers to the anomalous process (14) with only the trivalent $e\mu\gamma$ vertex and the Wilson coefficients $C_{eAL} = C_{eAR} = 1$. Similarly, $\sigma_{\gamma\gamma}^{(4)}$ refers to (14) through the $e\mu\gamma\gamma$ vertex and the coefficients $C_{eAAL} = C_{eAAR} = 1$. The numerical results agree with (9).

We expect the results for cross sections with cuts in Table 5 to be quite realistic, although detector efficiencies and acceptances have not been allowed for in those results. However, we expect the rapidity acceptance effects to be taken into account by the cut C_3 in (17), and we also expect the efficiency for photon identification to be no less than 90%, so that detector effects should be modest. The important exception to this, however, is the background process (16), which in Table 5 seems to represent one-third of $\sigma_{\gamma\gamma}^{(4)}$, but which must actually be adjusted for the electron-photon misidentification probability. In order to settle this

Table 5: Cumulative effects of the cuts (17) on the cross sections for (14), (15), and (16) at $E_e = 100$ GeV, $E_\mu = 3$ TeV.

$\mathcal{P}_\mu$	$\mathcal{P}_e$	Cuts	$\sigma_{\gamma\gamma}^{(3)}$ (fb)	$\sigma_{\gamma\gamma}^{(4)}$ (fb)	$\sigma_{\nu\nu\gamma\gamma}$ (fb)	$\sigma_{\nu\nu ee}$ (fb)
0.0	0.0	C_0	2.16	0.0103	770.2	426.6
0.0	0.0	$C_{0,1}$	2.16	0.0103	0.0049	0.073
0.0	0.0	$C_{0,1,2}$	2.16	0.0103	0.0015	0.0081
0.0	0.0	C_{0-3}	2.04	0.0097	3.23×10^{-5}	0.00108
+0.4	+0.8	$C_{0,1}$	2.86	0.0136	0.0014	0.081
+0.4	+0.8	$C_{0,1,2}$	2.69	0.0128	0.00043	0.0082
+0.4	+0.8	C_{0-3}	2.69	0.0128	9.85×10^{-6}	0.0038

issue, we carried out a detector simulation using Delphes 3.4 [41].

An $e^-\mu^+$ collider is highly asymmetric, so we assume its detector to have a correspondingly asymmetric design. We obtain a simple but effective asymmetric detector simulation in the lab frame by assuming that in the CM frame, in which the $e^-\mu^+$ collisions are forward-backward symmetric on average, the detector possesses the same capabilities as the symmetric Muon Collider detector implemented in Delphes 3.4 (which corresponds to the configuration file cards/delphes_card_MuonColliderDet.tcl in the Delphes distribution). We simulate the collisions with madgraph 5 with a loosened version of the cuts (17) in order to adequately populate the phase space,

$$
\begin{aligned}
C'_0 &= C_0, \quad C'_1 : E_3^*, E_4^* > 250.0\,\text{GeV}, \\
C'_2 &: p_T^{\text{tot}} = \left|\vec{p}_{3T} + \vec{p}_{4T}\right| < 40.0\,\text{GeV}, \quad C'_3 = \varnothing.
\end{aligned}
\tag{18}
$$

We run Pythia 6 [42] on these events for QED showering, followed by Delphes 3.4 with Muon Collider configuration. In Figure 3, we display normalized differential cross sections with respect to the CM rapidity y^*, the transverse momentum p_T, and the CM energy E^* for the final-state photons in processes (14) and (15), and the final-state $e^\pm$ for (16), at three different collision energies. Those differential cross sections correspond to detector-level events generated with the cuts (18) at the parton level. We notice here that the differential cross sections shown in the figure for the signal process (14) correspond to the contact interaction (7) represented by the symbol $\sigma_{\gamma\gamma}^{(4)}$ in Tables 5 and 6. For the kinematic variables considered in Figure 3, however, identical results would have been obtained with the interaction (6). We also point out here the good agreement of the analytical rapidity distribution (12) with the Monte Carlo data in Figure 3(c).

We then apply a preselection cut

$$
N_\gamma \geq 2, \quad N_{e^\pm} = 0,
\tag{19}
$$

to the Delphes events. Notice that (19) implicitly includes a cut in absolute rapidity $|y^*| < 2.5$, corresponding to the detector rapidity acceptance range. Finally, we apply the cuts

TABLE 6: Cross sections in fb for the signal processes (14) obtained from the operator Q_{eA}, see equation (6) and Figure 1(a); (14) obtained from the operator Q_{eAA}, see equation (7) and Figure 1(b); and the background processes (15) and (16). All cross sections, at the three energies shown, obtained at the detector-simulation level with cuts C_{0-3} from (17).

$\mathscr{P}_\mu$	$\mathscr{P}_e$	$\sigma_{\gamma\gamma}^{(3)}$ (fb)	$\sigma_{\gamma\gamma}^{(4)}$ (fb)	$\sigma_{\nu\nu\gamma\gamma}$ (fb)	$\sigma_{\nu\nu ee}$ (fb)
		$E_e = 100$ GeV, $E_\mu = 3$ TeV			
0.0	0.0	1.72	0.0082	$\sim 10^{-5}$	$\sim 10^{-5}$
+0.4	+0.8	2.26	0.011	$\lesssim 10^{-5}$	$\lesssim 10^{-5}$
		$E_e = 150$ GeV, $E_\mu = 4.5$ TeV			
0.0	0.0	1.61	0.039	$\sim 10^{-4}$	$\sim 10^{-5}$
+0.4	+0.8	2.12	0.051	$\lesssim 10^{-4}$	$\lesssim 10^{-5}$
		$E_e = 200$ GeV, $E_\mu = 6$ TeV			
0.0	0.0	1.46	0.11	$\sim 10^{-4}$	$\lesssim 10^{-5}$
+0.4	+0.8	1.93	0.15	$\lesssim 10^{-4}$	$\lesssim 10^{-5}$

C_{0-3} from (17) to the preselected events. The cross sections obtained for the detector-level events are summarized in Table 6. We notice here that the cross section for the process (14) induced by the dim 6 operator (6), as displayed by the diagrams in Figure 1(a), has an energy-independent cross section at the parton level but shows a slight decrease with increasing $\sqrt{s}$ in Table 6. This is due to the fact that the upper limit on p_T^{tot} we are using in (17) is fixed. This effect, however, is more than compensated for by the increase in the partonic cross section in the case of the signal process induced by the dim 8 operator (7), as displayed in Figure 1(b), leading to a increasing cross section also at the detector level. The cross section for the process (15) shows a very modest growth with $\sqrt{s}$ in Table 6, and process (16) actually decreases at the highest energy.

Furthermore, comparing the results in Table 6 at $(E_e, E_\mu) = (100, 3000)$ GeV with those in Table 5, we see that detector effects result in an effective efficiency of 84% for the $\gamma\gamma$ production processes given in the tables by $\sigma_{\gamma\gamma}^{(3)}$ and $\sigma_{\gamma\gamma}^{(4)}$. We see also that detector efficiencies reduce the cross section for the e^-e^+ background process (16) to the same $O(10^{-5})$ fb level as the $\gamma\gamma$ background (15). Completely analogous results are obtained at the two higher energies considered in Table 6.

4. Conclusions

We have obtained individual limits on LFV four fermion operators by looking at the two-to-two production processes they induce at the $e^-\mu^+$ collider. For operators $e\mu f\bar{f}$ where f is a second or third family fermion, the sensitivity of the collider is of the same order of magnitude as, and for some operators even somewhat stronger than, that of the $\mu A \longrightarrow eA$ conversion in nuclei. On the other hand, the $e\mu$ collider would have higher sensitivity than the other low energy

measurements $\mu \longrightarrow e\bar{e}e$ and $\mu \longrightarrow e\gamma$ even for first family fermions. In the particular case of the Wilson coefficients $C_{lq}^{(1,3)}$, for example, the expected sensitivity at an $e\mu$ collider would be at least as strong as that of all low-energy measurements, and an order of magnitude larger than that projected for Drell-Yan processes at the HL-LHC. This leads us to expect that, given the large number of independent effective four-fermion operators, the additional information obtained from the collider will certainly be invaluable. In the case of $e\mu \longrightarrow \gamma\gamma$ production, the limits from the collider are significantly more stringent than those from the low energy processes for the case of the dimension 8 $e\mu\gamma\gamma$ contact operator (7).

In the SM, the $f\bar{f}$ and $\gamma\gamma$ production involves an additional pair of neutrinos, and this makes the separation of signal and background straightforward. We have made a detailed analysis of background and signal for the case of $\gamma\gamma$ production, including detector simulation. We observe that with appropiate cuts on the photon energies, the photon pair transverse momentum and the photon rapidities we can dramatically lower the SM background with very little reduction of the signal.

We point out, finally, that our conclusions are based on the assumptions of an integrated luminosity of 1 ab^{-1} and beam energies $(E_e, E_\mu) = (100$ GeV, 3 TeV$)$, $(150$ GeV, 4.5 TeV$)$, $(200$ GeV, 6 TeV$)$, respectively. Clearly, higher luminosities and/or beam energies would lead to stronger sensitivities to the contact-interaction effective couplings considered here.

Data Availability

The data used to support the findings of this study are included within the article.

Disclosure

Conflicts of Interest

The authors declare that they have no conflicts of interest.

Acknowledgments

References

[1] R. Franceschini and M. Greco, "Higgs and BSM physics at the future muon collider," *Symmetry*, vol. 13, no. 5, p. 851, 2021.

[2] K. Cheung and Z. S. Wang, "Physics potential of a muon-proton collider," *Physical Review D*, vol. 103, no. 11, article 116009, 2021.

[3] D. Acosta and W. Li, "A muon-ion collider at BNL: the future QCD frontier and path to a new energy frontier of $\mu^+\mu^-$ colliders," 2021, https://arxiv.org/abs/2107.02073.

[4] T. Aoyama, N. Asmussen, M. Benayoun et al., "The anomalous magnetic moment of the muon in the standard model," *Physics Reports*, vol. 887, pp. 1–166, 2020.

[5] P. Banerjee, C. M. Carloni Calame, M. Chiesa et al., "Theory for muon-electron scattering @ 10 ppm," *The European Physical Journal C*, vol. 80, no. 6, p. 591, 2020.

[6] A. Masiero, P. Paradisi, and M. Passera, "New physics at the MUonE experiment at CERN," *Physical Review D*, vol. 102, no. 7, article 075013, 2020.

[7] G. Abbiendi, C. M. C. Calame, U. Marconi et al., "Measuring the leading hadronic contribution to the muon g-2 via μe scattering," *European Physical Journal C*, vol. 77, no. 3, p. 139, 2017.

[8] C. M. Carloni Calame, M. Passera, L. Trentadue, and G. Venanzoni, "A new approach to evaluate the leading hadronic corrections to the muon g-2," *Physics Letters B*, vol. 746, pp. 325–329, 2015.

[9] B. Abi, T. Albahri, S. al-Kilani et al., "Measurement of the positive muon anomalous magnetic moment to 0.46 ppm," *Physical Review Letters*, vol. 126, no. 14, article 141801, 2021.

[10] J. Ellis, J. L. Evans, N. Nagata, D. V. Nanopoulos, and K. A. Olive, "Flipped $g_\mu - 2$," https://arxiv.org/abs/2107.03025.

[11] N. Arkani-Hamed and K. Harigaya, "Naturalness and the muon magnetic moment," 2021, https://arxiv.org/abs/2106.01373.

[12] A. Greljo, Y. Soreq, P. Stangl, A. E. Thomsen, and J. Zupan, "Muonic force behind flavor anomalies," 2021, https://arxiv.org/abs/2107.07518.

[13] A. Aboubrahim, P. Nath, and R. M. Syed, "Yukawa coupling unification in an SO(10) model consistent with Fermilab (g–2) result," *Journal of High Energy Physics*, vol. 2021, article 2, 2021.

[14] P. Athron, C. Balázs, D. H. Jacob, W. Kotlarski, D. Stöckinger, and H. Stöckinger-Kim, "New physics explanations of a_μ in light of the FNAL muon $g - 2$ measurement," 2021, https://arxiv.org/abs/2104.03691.

[15] J. S. Alvarado, S. F. Mantilla, R. Martinez, and F. Ochoa, "A non-universal $U(1)_X$ extension to the standard model to study the B meson anomaly and muon $g - 2$," https://arxiv.org/abs/2105.04715.

[16] A. E. Cárcamo Hernández, C. Espinoza, J. Carlos Gómez-Izquierdo, and M. Mondragón, "Fermion masses and mixings dark matter leptogenesis and $g - 2$ muon anomaly in an extended 2HDM with inverse seesaw," 2021, https://arxiv.org/abs/2104.02730.

[17] A. Crivellin, C. Greub, D. Müller, and F. Saturnino, "Scalar leptoquarks in leptonic processes," 2021, https://arxiv.org/abs/2010.06593.

[18] R. Bonciani, A. Broggio, S. Di Vita et al., "The two-loop four-fermion scattering amplitude in QED," 2021, https://arxiv.org/abs/2106.13179.

[19] M. Heller, "Planar two-loop integrals for μe scattering in QED with finite lepton masses," https://arxiv.org/abs/2105.08046.

[20] S. Y. Choi, C. S. Kim, Y. J. Kwon, and S. H. Lee, "High-energy FCNC search through e mu colliders," *Physical Review D*, vol. 57, pp. 7023–7026, 1998.

[21] V. D. Barger, S. Pakvasa, and X. Tata, "Are e mu colliders interesting?," *Physics Letters B*, vol. 415, pp. 200–204, 1997.

[22] J. C. Montero, V. Pleitez, and M. C. Rodriguez, "Left-right asymmetries in polarized e-u scattering," *Physical Review D*, vol. 58, article 097505, 1998.

[23] G. Cvetic and C. S. Kim, "Heavy Majorana neutrino production at electron - muon colliders," *Physics Letters B*, vol. 461, pp. 248–255, 1999.

[24] F. M. L. Almeida Jr., Y. do Amaral Coutinho, J. A. M. Simoes, and M. A. B. Valedo, "Single neutral heavy lepton production at electron muon colliders," *Physics Letters B*, vol. 494, pp. 273–279, 2000.

[25] J. K. Singhal, S. Singh, and A. K. Nagawat, "Possible exotic neutrino signature in electron muon collisions," 2007, https://arxiv.org/abs/0703136.

[26] F. Bossi and P. Ciafaloni, "Lepton flavor violation at muon-electron colliders," *Journal of High Energy Physics*, vol. 2020, article 33, 2020.

[27] M. Lu, A. M. Levin, C. Li et al., "The physics case for an electron-muon collider," *Advances in High Energy Physics*, vol. 2021, Article ID 6693618, 6 pages, 2021.

[28] S. Davidson, "Completeness and complementarity for $\mu \longrightarrow e\gamma\mu \longrightarrow e\bar{e}e$ and $\mu A \longrightarrow eA$," 2021, https://arxiv.org/abs/2010.00317.

[29] M. Ardu and S. Davidson, "What is leading order for LFV in SMEFT?," 2021, https://arxiv.org/abs/2103.07212.

[30] S. Davidson, Y. Kuno, Y. Uesaka, and M. Yamanaka, "Probing $\mu e\gamma\gamma$ contact interactions with $\mu \longrightarrow e$ conversion," *Physical Review D*, vol. 102, no. 11, article 115043, 2020.

[31] B. Grzadkowski, M. Iskrzynski, M. Misiak, and J. Rosiek, "Dimension-six terms in the standard model Lagrangian," *Journal of High Energy Physics*, vol. 2010, article 85, 2010.

[32] M. L. Mangano and S. J. Parke, "Multi-parton amplitudes in gauge theories," *Physics Reports*, vol. 200, pp. 301–367, 1991.

[33] The SINDRUM II Collaboration, W. Bertl, R. Engfer et al., "A search for μ-e conversion in muonic gold," *European Physical Journal C: Particles and Fields*, vol. 47, no. 2, pp. 337–346, 2006.

[34] R. Alonso, E. E. Jenkins, A. V. Manohar, and M. Trott, "Renormalization group evolution of the standard model dimension six operators III: gauge coupling dependence and phenomenology," *Journal of High Energy Physics*, vol. 2014, article 159, 2014.

[35] E. E. Jenkins, A. V. Manohar, and M. Trott, "Renormalization group evolution of the standard model dimension six operators II: Yukawa dependence," *Journal of High Energy Physics*, vol. 2014, article 35, 2014.

[36] E. E. Jenkins, A. V. Manohar, and M. Trott, "Naive dimensional analysis counting of gauge theory amplitudes and anomalous dimensions," *Physics Letters B*, vol. 726, no. 4-5, pp. 697–702, 2013.

[37] E. E. Jenkins, A. V. Manohar, and M. Trott, "Renormalization group evolution of the standard model dimension six operators I: formalism and lambda dependence," *Journal of High Energy Physics*, vol. 2013, article 87, 2013.

[38] A. Angelescu, D. A. Faroughy, and O. Sumensari, "Lepton flavor violation and dilepton tails at the LHC," *The European Physical Journal C*, vol. 80, no. 7, p. 641, 2020.

[39] A. Alloul, N. D. Christensen, C. Degrande, C. Duhr, and B. Fuks, "FeynRules 2.0 – a complete toolbox for tree-level phenomenology," *Computer Physics Communications*, vol. 185, pp. 2250–2300, 2014.

[40] J. Alwall, M. Herquet, F. Maltoni, O. Mattelaer, and T. Stelzer, "MadGraph 5 : going beyond," *Journal of High Energy Physics*, vol. 2011, article 128, 2011.

[41] J. De Favereau, C. Delaere, P. Demin et al., "Delphes 3 a modular framework for the fast simulation of a generic collider experiment," *Journal of High Energy Physics*, vol. 2014, article 57, 2014.

[42] T. Sjöstrand, S. Mrenna, and P. Skands, "Pythia 6.4 physics and manual," *Journal of High Energy Physics*, vol. 2006, article 26, 2006.